Electronic Supplementary Material (ESI) for Journal of Materials Chemistry A.

Supplementary Information

Discovery of low-temperature GeTe-based thermoelectric alloys with high performance competing with Bi_2Te_3

Longquan Wang[#], Junqin Li[#], Chunxiao Zhang, Teng Ding, Yucheng Xie, Yu Li, Fusheng Liu, Weiqin Ao and Chaohua Zhang*

College of Materials Science and Engineering, Shenzhen Key Laboratory of Special Functional Materials, Shenzhen Engineering Laboratory for Advanced Technology of Ceramics, Guangdong Research Center for Interfacial Engineering of Functional Materials, Institute of Deep Underground Sciences and Green Energy, Shenzhen University, Shenzhen 518060, P. R. China

[#] Author contributed equally to this work

E-mail: zhangch@szu.edu.cn

Computational methods:

The results were obtained in calculations using the (2×2×2) supercell models. The primitive cell of GeTe is also used for comparation. Therefore, the cell parameters of the cubic GeTe-based supercell are set as 12.023 Å. The geometry structure of (bulk GeTe) was optimized using density functional theory (DFT) implemented in the Vienna *ab initio* simulation package (VASP)[1]. The Perdew-Burke-Ernzerhof exchange correlation functional (GGA-PBE)[2] and the projector augmented wave (PAW)[3] type Pseudopotentials were employed. The cut-off energy of the plane-wave basis was set to be 500 eV, and the atomic positions were fully relaxed until the forces on all atoms were less than 10^{-2} eV/Å. The energy convergence criterion was set to be 10^{-5} eV/cell. A dense k-mesh of 2 ×2×2 sampling with the Monkhorse-Pack model[4] was used for the Brillouin zone (BZ) integration. In this work, the spin-orbit coupling (SOC) effects were considered in the calculations of band structure and thermoelectric properties of (bulk GeTe). The symmetry **k**-points of orthorhombic lattice are list below:

$\times\mathbf{b}_1$	$\times\mathbf{b}_2$	$\times\mathbf{b}_3$		$\times\mathbf{b}_1$	$\times\mathbf{b}_2$	$\times\mathbf{b}_3$	
0	0	0	**Γ**	-1/2	0	1/2	**M**
-1/2	1/2	1/2	**R**	-1/2	0	0	**X**
0	0	1/2	**Z**	0	1/2	1/2	**Q**

Table S1. X-ray Fluorescence (XRF) characterization of the $(Ge_{0.87}Pb_{0.13}Te)_{1-x}(Bi_2Te_3)_x$ alloys before and after quenching (x=0.05, x=0.07).

Element	B5-C	B5-LN	B7-C	B7-LN
Te	0.497	0.497	0.504	0.505
Ge	0.413	0.416	0.395	0.393
Pb	0.052	0.050	0.050	0.051
Bi	0.038	0.037	0.051	0.051

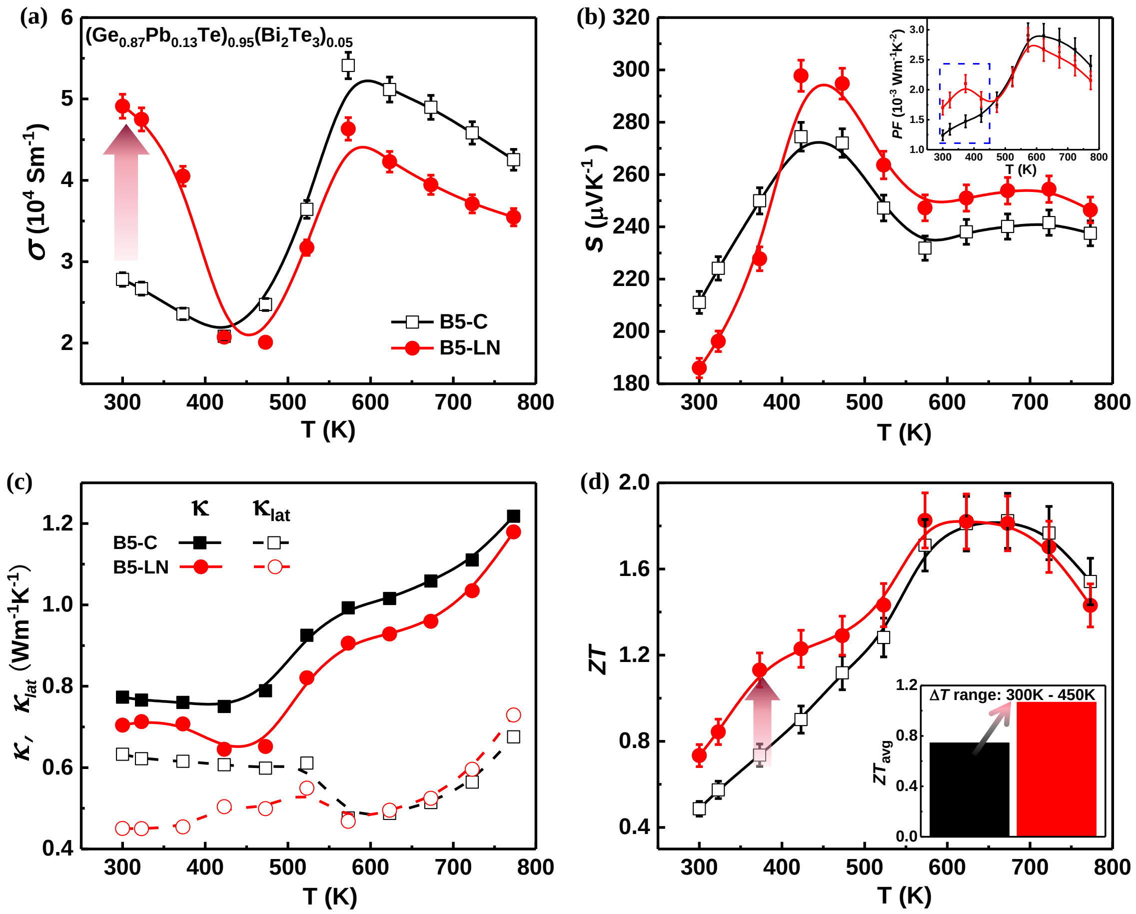

Figure S1. The reproducibility of the temperature-dependent thermoelectric properties of the $(Ge_{0.87}Pb_{0.13}Te)_{0.95}(Bi_2Te_3)_{0.05}$ with/without quenching treatment. **(a)** Electrical conduct ivity, **(b)** Seebeck coefficient, **(c)** total and lattice thermal conductivity, **(d)** figure of merit ZT. The inset of (b) and (d) display the corresponding power factor PF and average ZT within 300-450 K.

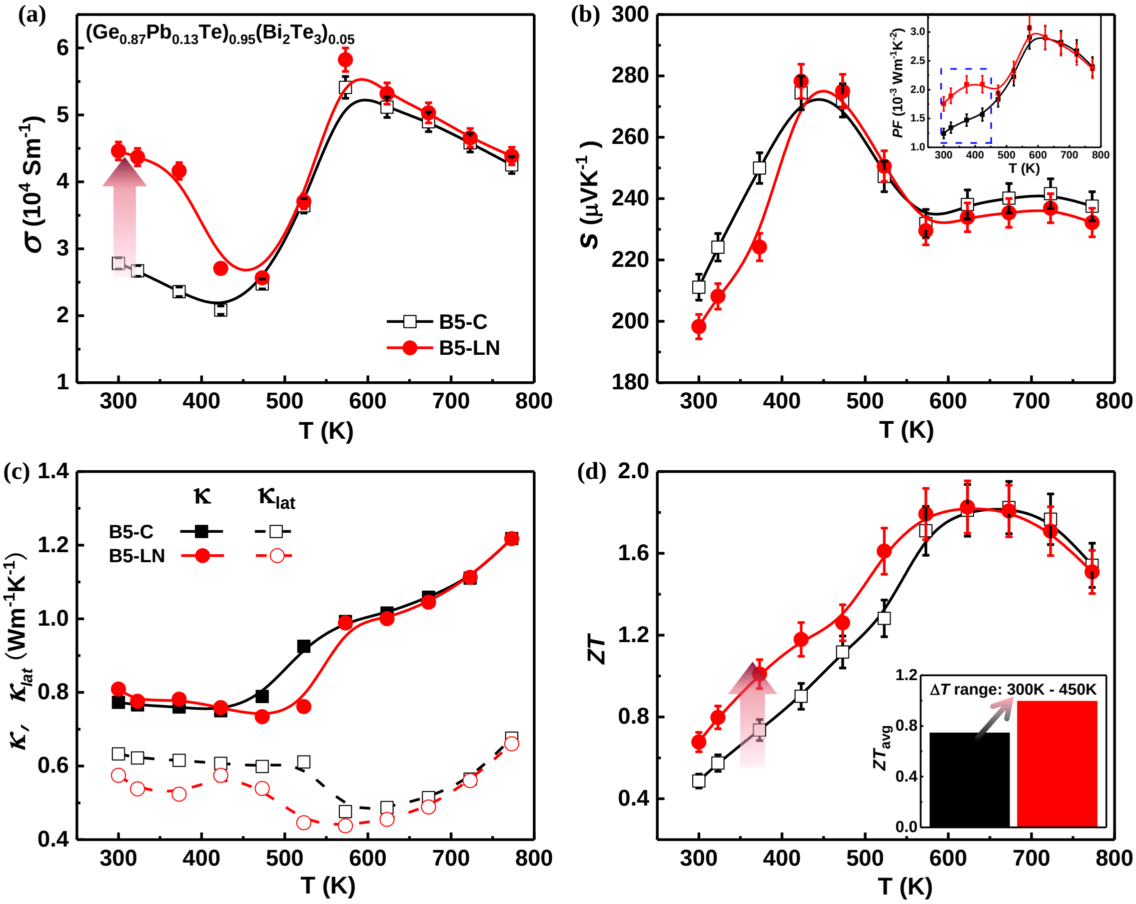

Figure S2. The reproducibility of the temperature-dependent thermoelectric properties of the $(Ge_{0.87}Pb_{0.13}Te)_{0.95}(Bi_2Te_3)_{0.05}$ samples with/without quenching treatment. **(a)** Electrical conductivity, **(b)** Seebeck coefficient, **(c)** total and lattice thermal conductivity, **(d)** figure of merit ZT. The inset of (b) and (d) display the corresponding power factor PF and average ZT within 300-450 K.

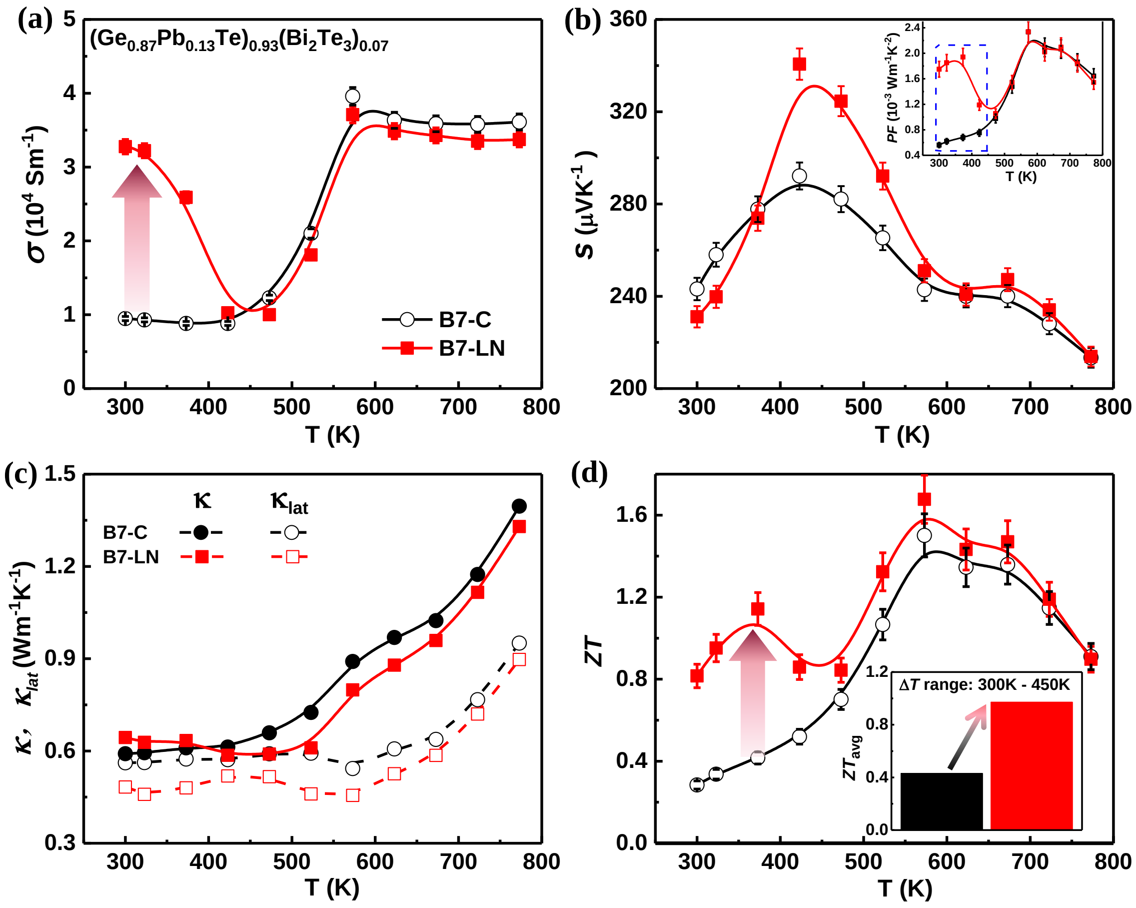

Figure S3. The reproducibility of the temperature-dependent thermoelectric properties of the $(Ge_{0.87}Pb_{0.13}Te)_{0.93}(Bi_2Te_3)_{0.07}$ samples with/without quenching treatment. **(a)** Electrical conductivity, **(b)** Seebeck coefficient, **(c)** total and lattice thermal conductivity, **(d)** figure of merit ZT. The inset of (b) and (d) display the corresponding power factor PF and average ZT within 300-450 K.

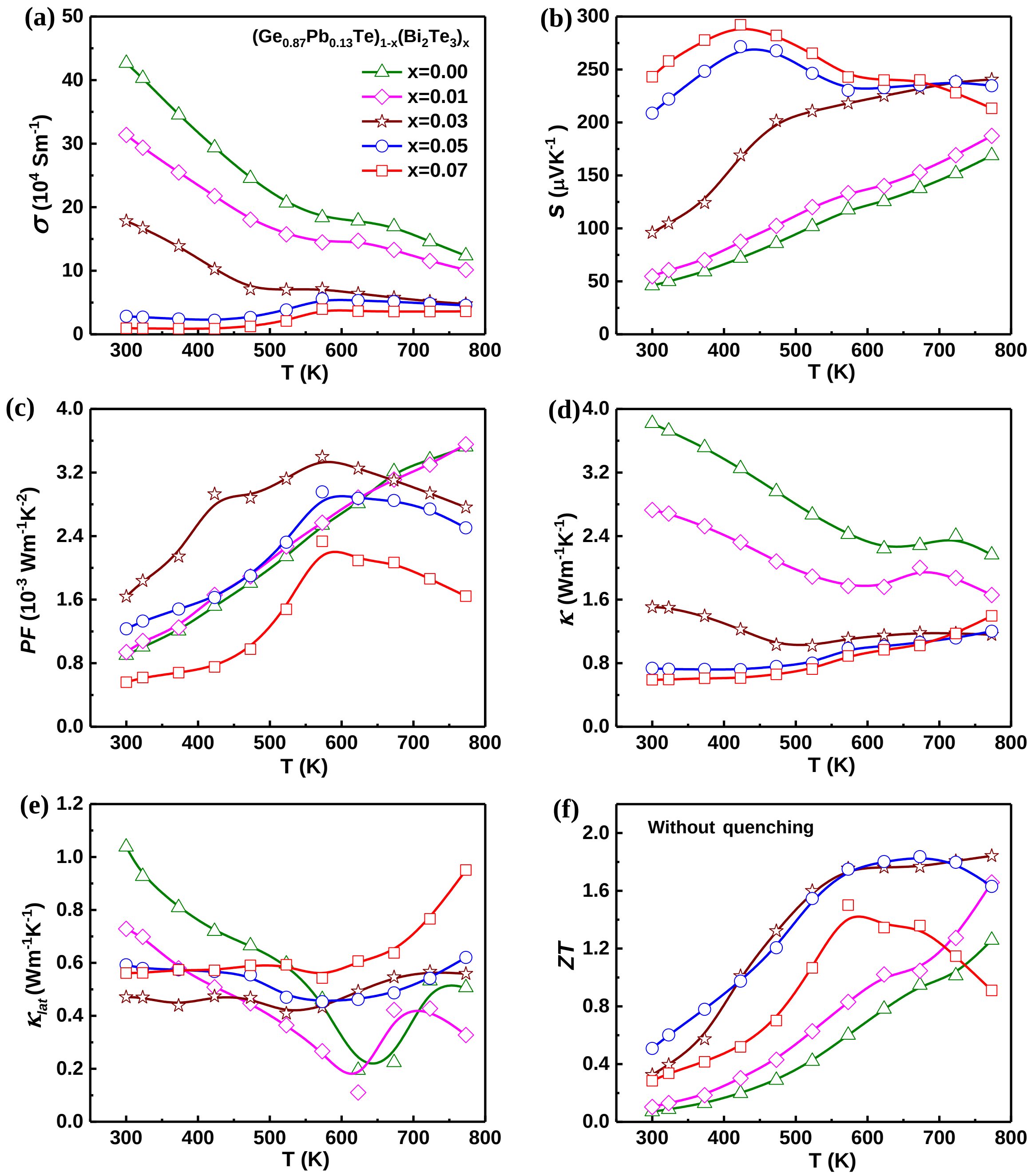

Figure S4. Temperature-dependent thermoelectric properties of the $(Ge_{0.87}Pb_{0.13}Te)_{1-x}(Bi_2Te_3)_x$ samples without quenching treatment. **(a)** Electrical conductivity, **(b)** Seebeck coefficient, **(c)** power factor **(d)** total thermal conductivity, **(e)** lattice thermal conductivity, and **(f)** ZT.

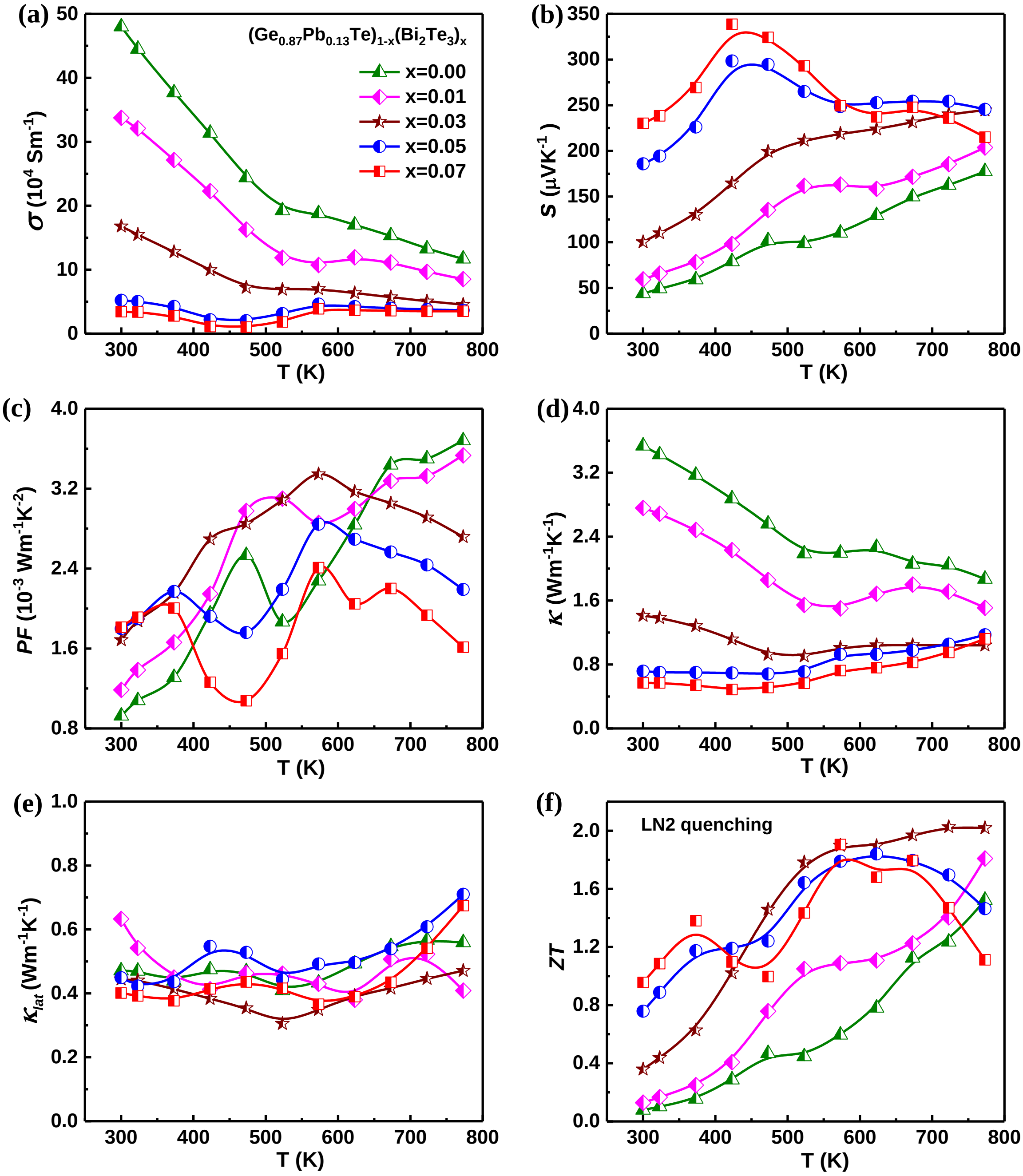

Figure S5. Temperature-dependent thermoelectric properties of the $(Ge_{0.87}Pb_{0.13}Te)_{1-x}(Bi_2Te_3)_x$ samples with quenching treatment. **(a)** Electrical conductivity, **(b)** Seebeck coefficient, **(c)** power factor **(d)** total thermal conductivity, **(e)** lattice thermal conductivity, and **(f)** ZT.

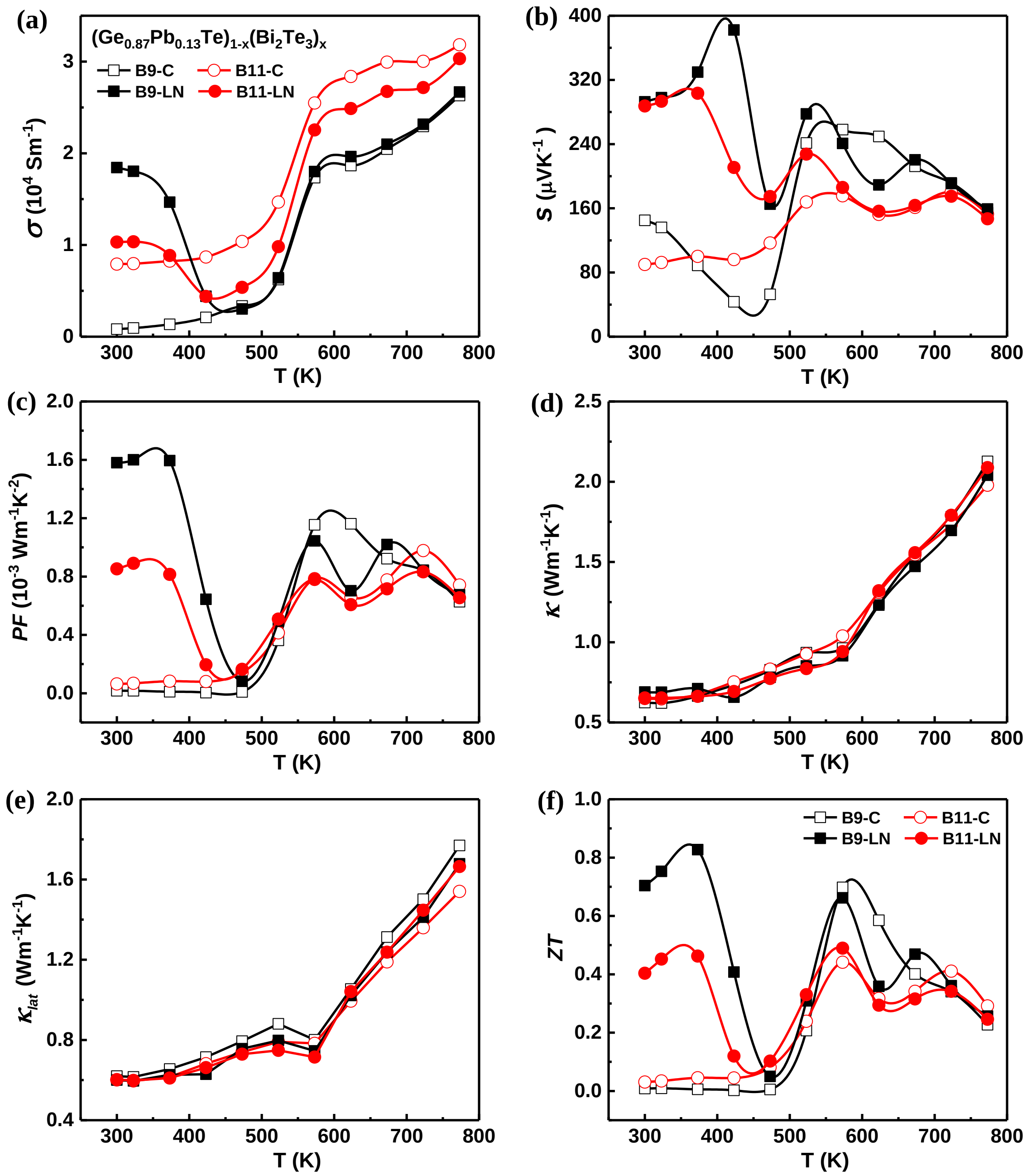

Figure S6. Temperature-dependent thermoelectric properties of the $(Ge_{0.87}Pb_{0.13}Te)_{1-x}(Bi_2Te_3)_x$ (x=0.09, 0.11) samples with/without quenching treatment. **(a)** Electrical conductivity, **(b)** Seebeck coefficient, **(c)** power factor **(d)** total thermal conductivity, **(e)** lattice thermal conductivity, and **(f)** ZT.

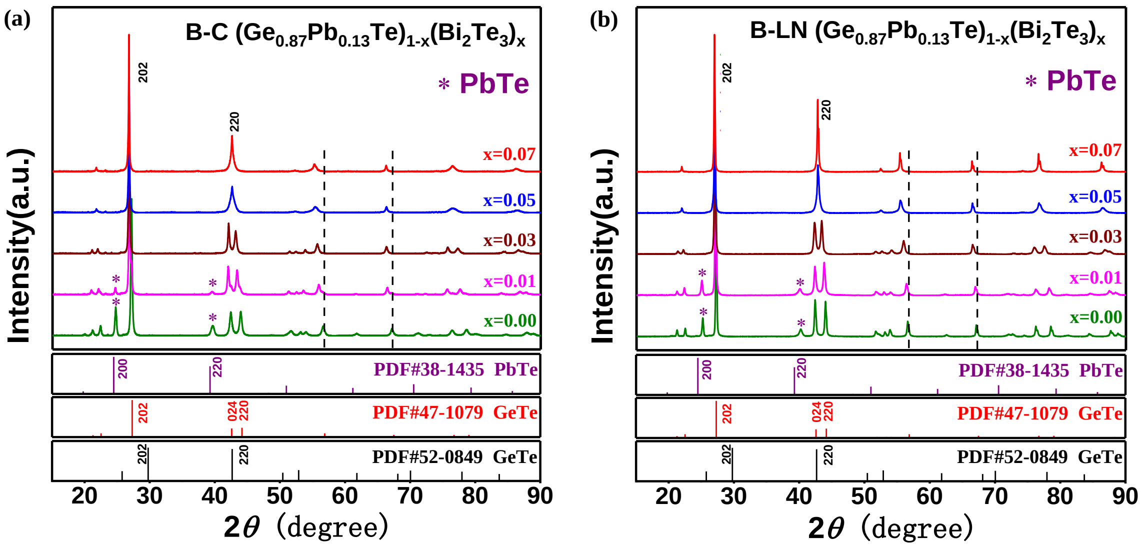

Figure S7. XRD patterns of $(Ge_{0.87}Pb_{0.13}Te)_{1-x}(Bi_2Te_3)_x$ alloys with different composition *x* **(a)** before quenching. **(b)** after quenching.

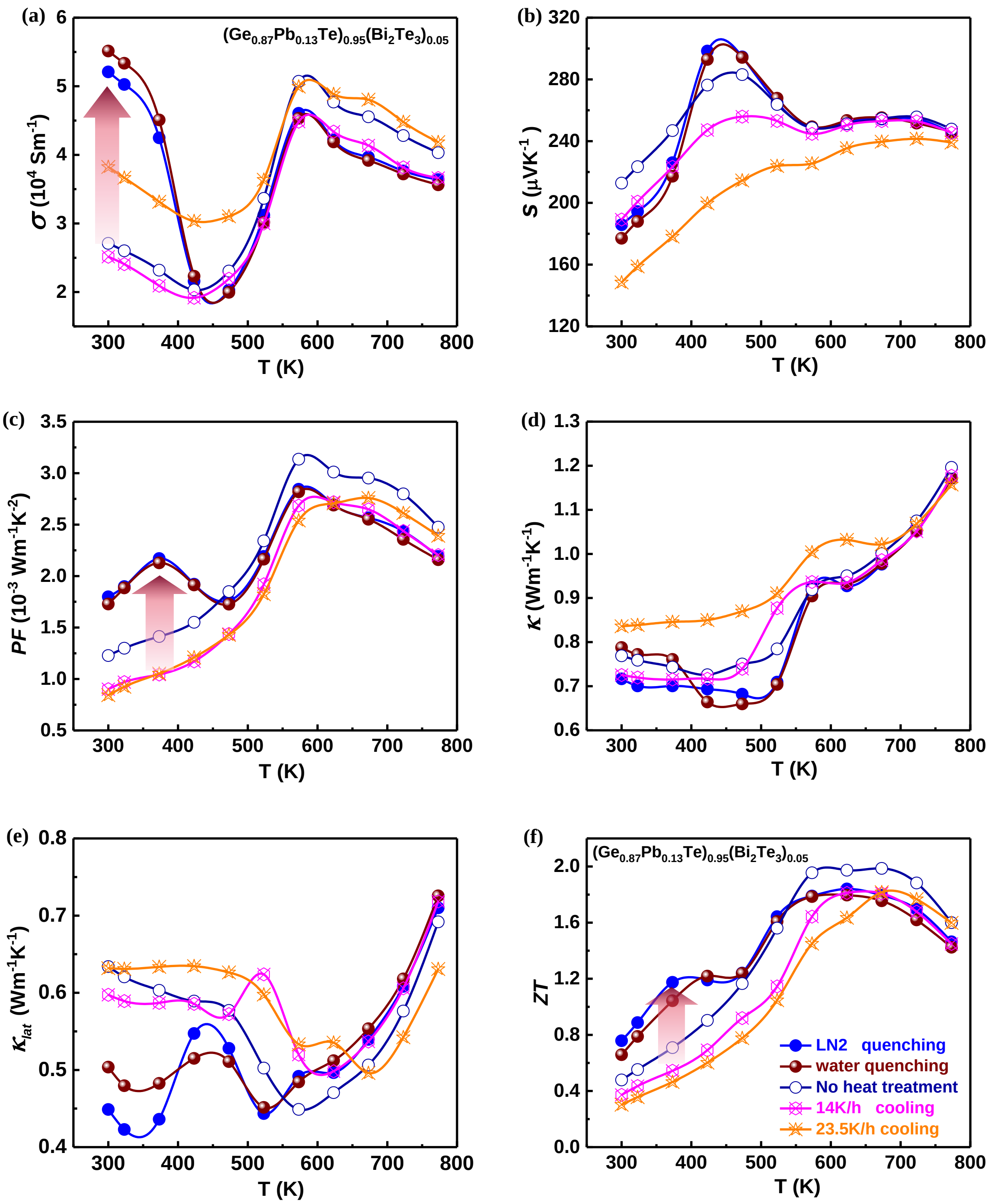

Figure S8. Temperature-dependent thermoelectric properties of the $(Ge_{0.87}Pb_{0.13}Te)_{0.95}(Bi_2Te_3)_{0.05}$ samples with different heat treatment (LN2 quenching, water quenching, slowing cooling with rate of 14 K/h and 23.5 K/h) and without heat treatment as well. **(a)** Electrical conductivity, **(b)** Seebeck coefficient, **(c)** power factor **(d)** total thermal conductivity, **(e)** lattice thermal conductivity, and **(f)** ZT.

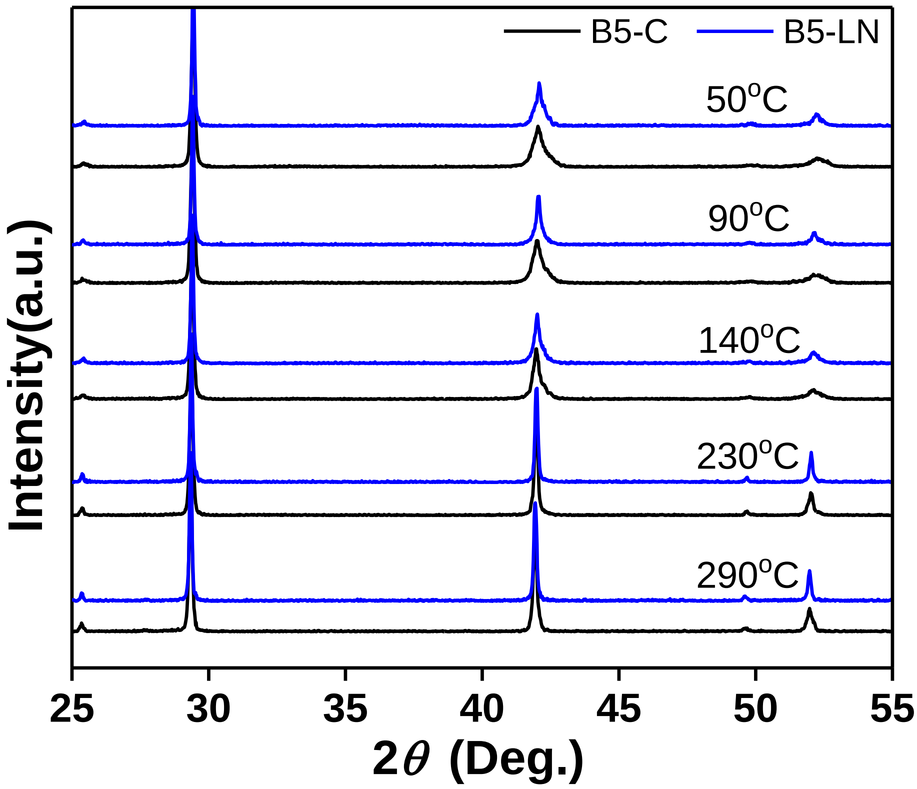

Figure S9. The temperature-dependent X-ray diffraction patterns of the B5-C and B5-LN samples from 50 °C to 290 °C, which are nearly the same with each other in each test temperature.

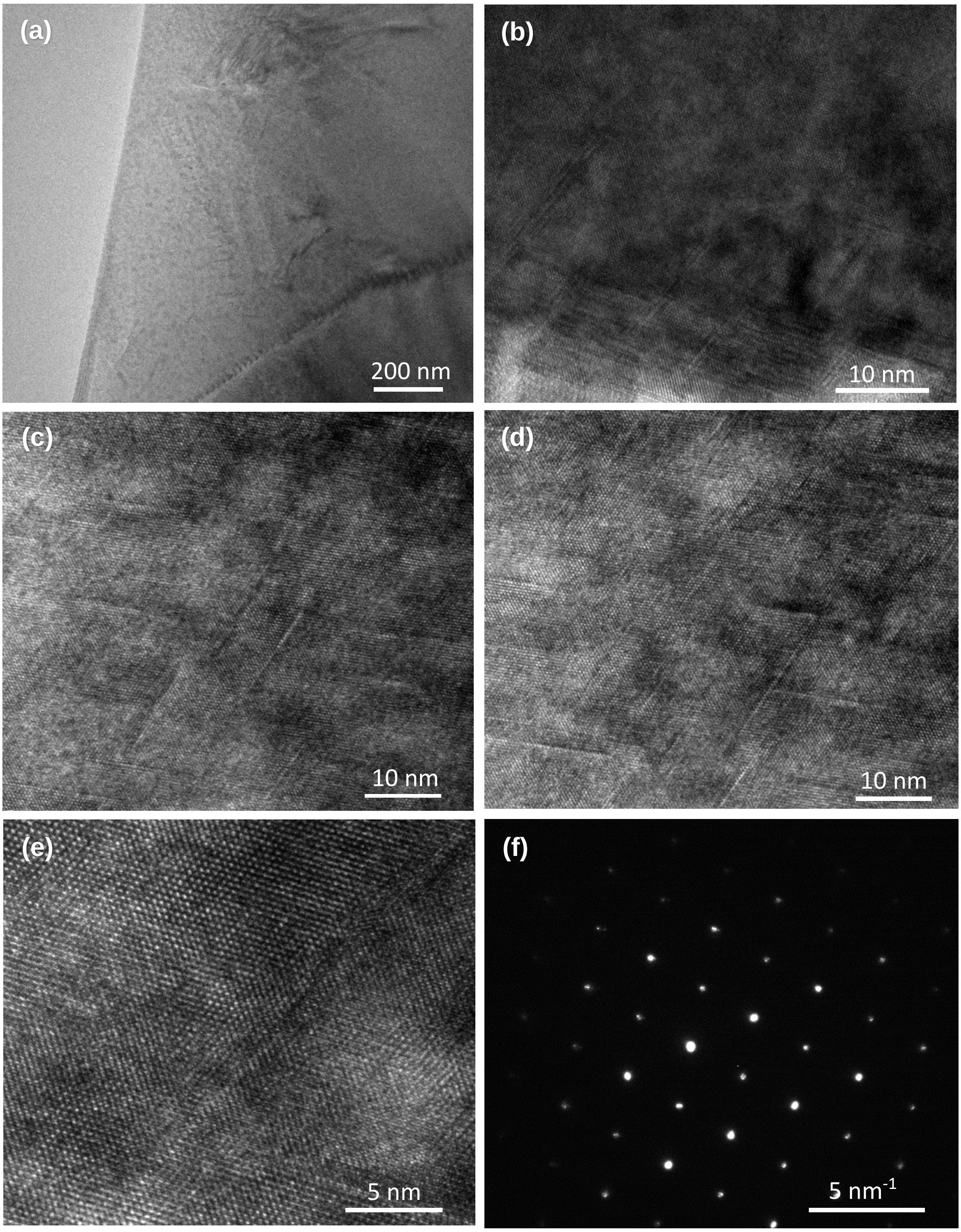

Figure S10. TEM characterizations of $(Ge_{0.87}Pb_{0.13}Te)_{0.95}(Bi_2Te_3)_{0.05}$ without quenching treatment (B5-C). **(a)** Low-magnification TEM image, **(b) (c) (d) (e)** High-resolution TEM (HRTEM) images and **(f)** the corresponding selected area electron diffraction (SAED) pattern in the examined region.

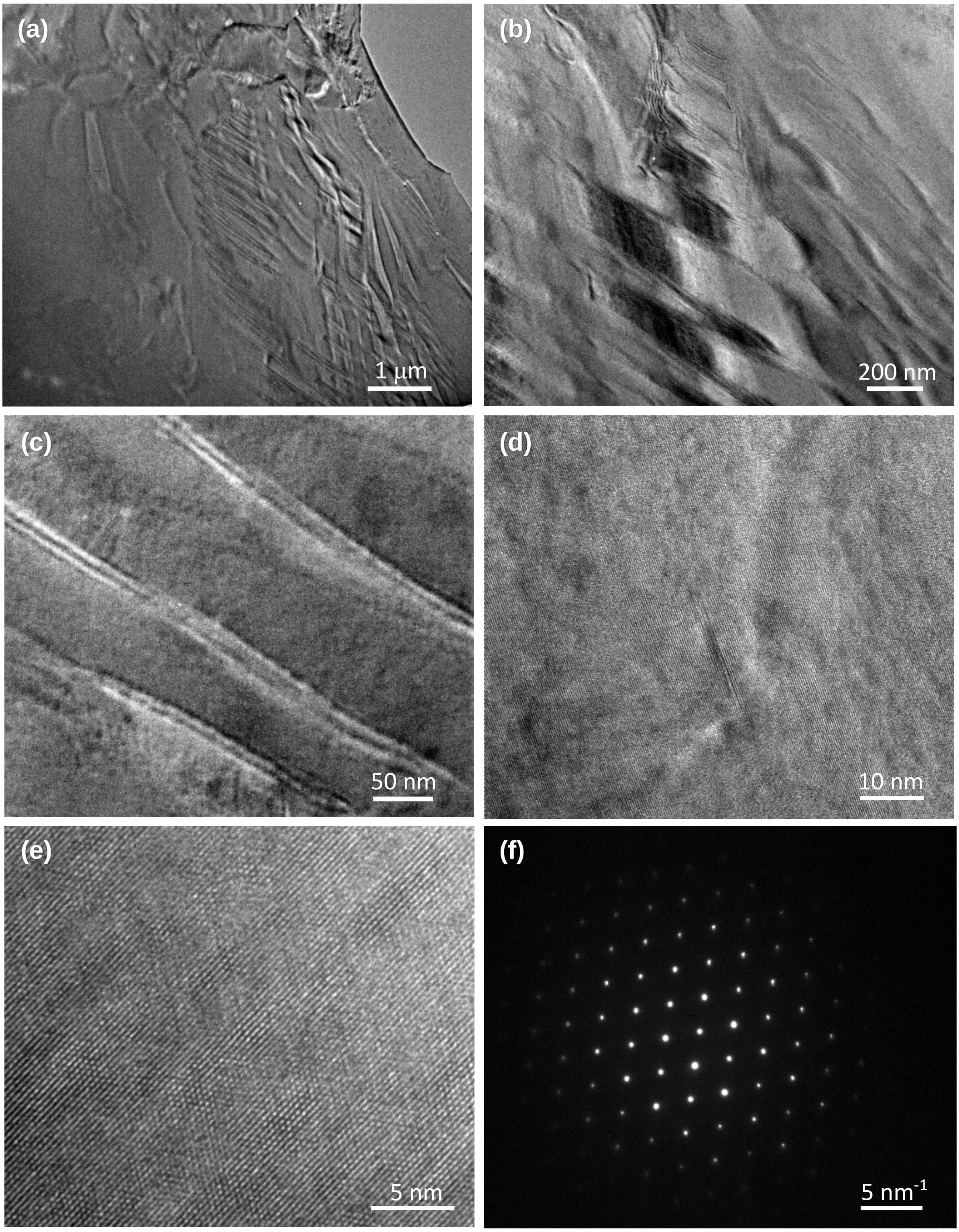

Figure S11. TEM characterizations of $(Ge_{0.87}Pb_{0.13}Te)_{0.95}(Bi_2Te_3)_{0.05}$ with quenching treatment (B5-LN). **(a)(b)(c)** Low-magnification TEM images, **(d)(e)** HRTEM images and **(f)** the corresponding selected area electron diffraction (SAED) pattern in the examined region.

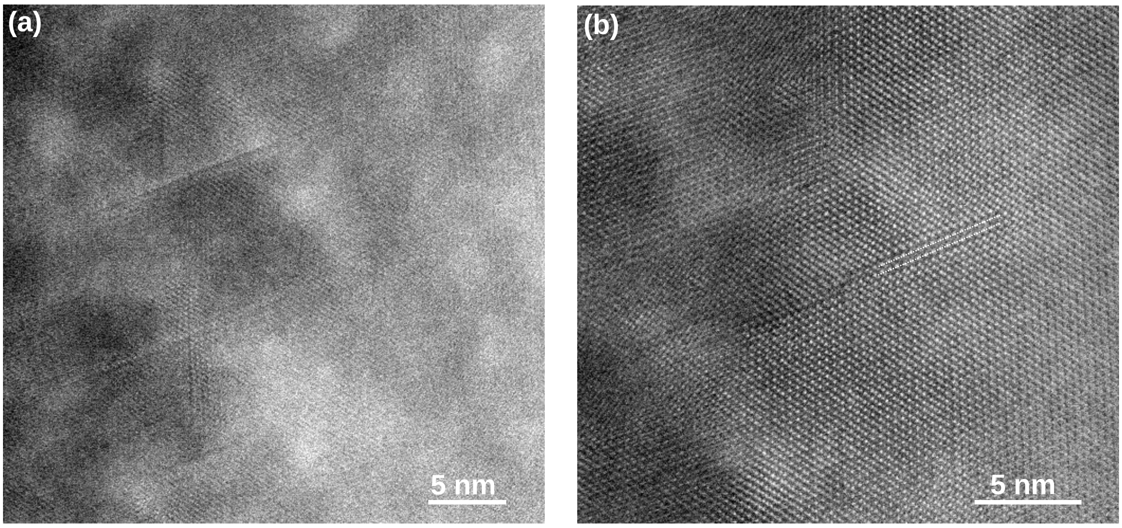

Figure S12. (a)(b) HAADF STEM characterizations of $(Ge_{0.87}Pb_{0.13}Te)_{0.95}(Bi_2Te_3)_{0.05}$ without quenching treatment (B5-C). Randomly distributed Ge vacancy arrays as highlighted with white dotted lines in Figure (b).

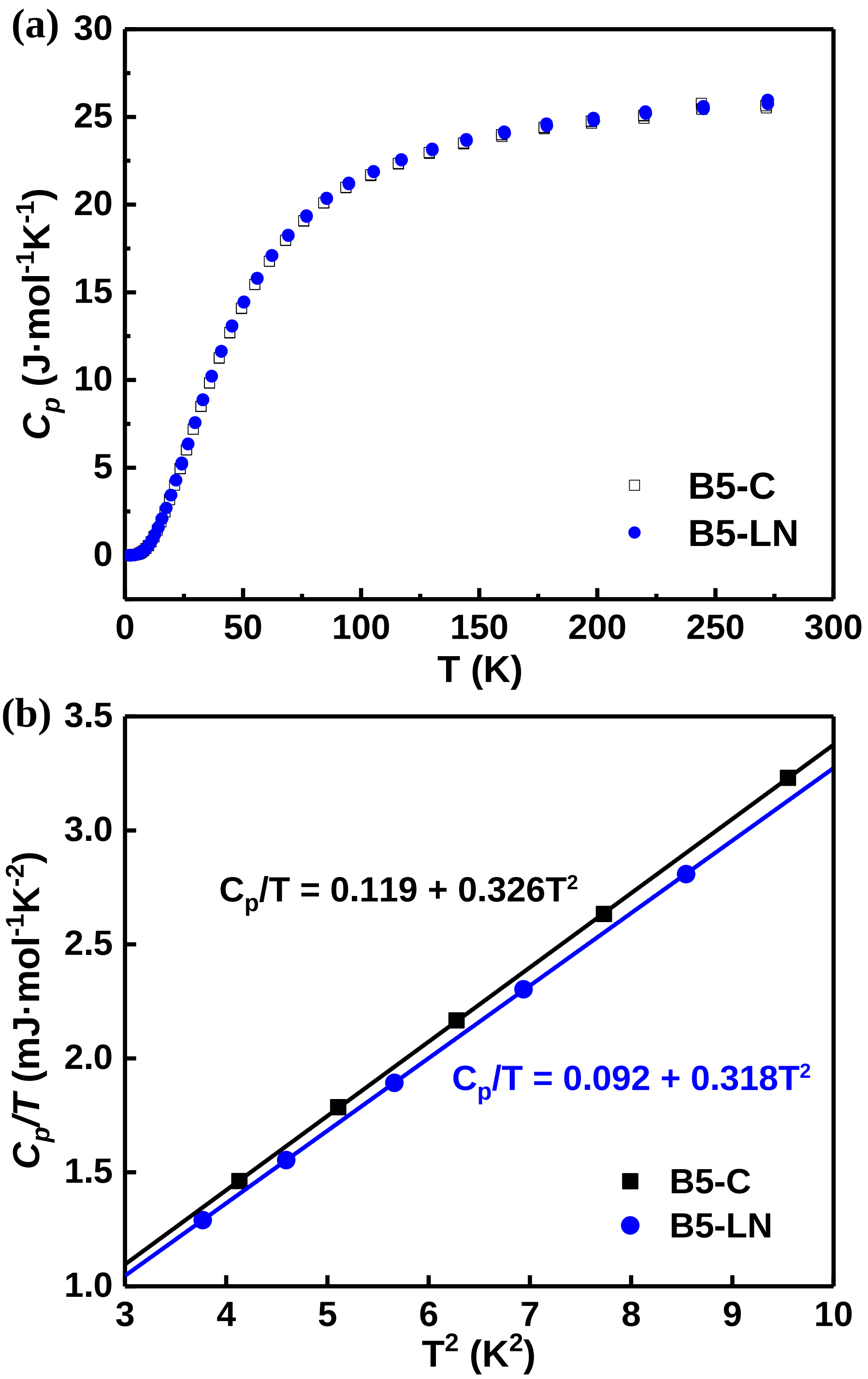

Figure S13. (a) The temperature-dependent heat capacity of the $(Ge_{0.87}Pb_{0.13}Te)_{0.95}(Bi_2Te_3)_{0.05}$ samples with/without quenching treatment (B5-C and B5-LN). **(b)** C_p/T vs T^2 plot in the 1.8-4 K range.

References

1 Kresse, G. & Furthmüller, J. Efficient iterative schemes for ab initio total-energy calculations using a plane-wave basis set. *Physical Review B* **54**, 11169-11186, (1996).

2 Perdew, J. P., Burke, K. & Ernzerhof, M. Generalized Gradient Approximation Made Simple. *Physical Review Letters* **77**, 3865-3868, (1996).

3 Kresse, G. & Joubert, D. From ultrasoft pseudopotentials to the projector augmented-wave method. *Physical Review B* **59**, 1758-1775, (1999).

4 Monkhorst, H. J. & Pack, J. D. Special points for Brillouin-zone integrations. *Physical Review B* **13**, 5188-5192, (1976).